Computational Mechanics (2022) 70:549–563
https://doi.org/10.1007/s00466-022-02178-7

ORIGINAL PAPER

Finite element methodology for modeling aircraft aerodynamics: development, simulation, and validation

Manoj R. Rajanna[1] · Emily L. Johnson[2] · David Codoni[3] · Artem Korobenko[3] · Yuri Bazilevs[4] · Ning Liu[5] · Jim Lua[5] · Nam Phan[6] · Ming-Chen Hsu[1]

Received: 18 February 2022 / Accepted: 3 April 2022 / Published online: 10 June 2022

Abstract
In this work, we propose and validate a new stabilized compressible flow finite element framework for the simulation of aerospace applications. The framework is comprised of the streamline upwind/Petrov–Galerkin (SUPG)-based Navier–Stokes equations for compressible flows, the weakly enforced essential boundary conditions that act as a wall function, and the entropy-based discontinuity-capturing equation that acts as a shock-capturing operator. The accuracy and robustness of the framework is tested for various Mach numbers ranging from low-subsonic to transonic flow regimes. The aerodynamic simulations are carried out for 2D and 3D validation cases of flow around the NACA 0012 airfoil, RAE 2822 airfoil, ONERA M6 wing, and NASA Common Research Model (CRM) aircraft. The pressure coefficients obtained from the simulations of all cases are compared with experimental data. The computational results show good agreement with the experimental findings and demonstrate the accuracy and effectiveness of the finite element framework presented in this work for the simulation of aircraft aerodynamics.

Keywords Compressible flow · Stabilized methods · Discontinuity capturing · Weak essential boundary conditions · NASA Common Research Model

1 Introduction

Over the years, numerous research and development efforts in the aerospace industry have been carried out to improve the fidelity of computational fluid dynamics (CFD) simulations. While most of the CFD work in aerodynamics is based on finite volume [1] or finite difference [2,3] methods, significant progress has also been made in the field of flow analysis using finite element methods [4], which are based on the weak or variational forms of the governing equations. In the 1970s, the success of finite element methods in structural mechanics encouraged their development to simulate flow physics problems. The first significant development was the streamline upwind/Petrov–Galerkin (SUPG) method for incompressible flows [5], which was later extended to compressible flows using conservation variables [6] and entropy variables [7–9]. The idea of SUPG was to add a residual-based stabilization term to the Galerkin form of the governing equations to improve the stability of the finite element method for simulating higher Reynolds number flows while preserving consistency of the formulation. Over the years, important progress was made in enhancing stabilized methods for compressible flow analysis [10–23], however, oscillations in the vicinity of shocks and other sharp solution features are often observed. To mitigate this challenge, shock- or discontinuity-capturing operators were proposed [24–35] to provide additional dissipation by adding solution- and mesh-dependent artificial viscosity terms to a stabilized formulation. These operators are often residual-based and

✉ Ming-Chen Hsu
jmchsu@iastate.edu

1 Department of Mechanical Engineering, Iowa State University, Ames, IA 50011, USA

2 Department of Aerospace and Mechanical Engineering, University of Notre Dame, Notre Dame, IN 46556, USA

3 Department of Mechanical and Manufacturing Engineering, University of Calgary, Calgary, AB T2N 1N4, Canada

4 School of Engineering, Brown University, Providence, RI 02912, USA

5 Global Engineering & Materials, Inc., Princeton, NJ 08540, USA

6 Structures Division, Naval Air Systems Command (NAVAIR), Patuxent River, MD 20670, USA

thus retain consistency of the formulation. A thorough review of stabilized methods and discontinuity-capturing techniques for compressible flows can be found in Hughes et al. [21].

Another critical development of the finite element method for fluid flow applications is the weak enforcement of no-slip conditions. Weak imposition of essential boundary conditions was introduced in Bazilevs et al. [36–38] for incompressible flows and later extended to compressible flows in Xu et al. [39]. Imposing the Dirichlet boundary conditions weakly allows a certain amount of flow to slip on the solid surface, which removes some of the burden from the boundary-layer mesh to resolve the sharp velocity gradients near the wall. This effect imitates the presence of a boundary layer that would otherwise need to be resolved with spatial refinement, allowing more accurate solutions on coarse boundary-layer meshes [39–43]. Note that the weak Dirichlet boundary conditions can be seen as a wall function, as investigated in Bazilevs et al. [37] and Golshan et al. [44]. More recently, weakly enforced no-slip conditions were developed and applied in the context of immersogeometric analysis [45–48], which led to solutions of higher-order accuracy on non-boundary-fitted meshes.

Many aerospace applications fall under compressible flow regimes and involve complex phenomena under different flow conditions. Following numerous developments in the compressible flow SUPG methodology, shock-capturing operator, and weakly enforced essential boundary conditions, finite element methods for compressible flows have been successfully applied to many aerospace applications, such as air intake of a jet engine with adjustable spool at supersonic speeds [13], delta-wing [13,39,49], commercial and fighter aircraft [13,50], missile [51], spacecraft parachute aerodynamics [22,23], gas turbines [39,52–54], UH-60 rotorcraft [47], and hypersonic flows [55].

The objective of this work is to improve and validate a finite element framework for 3D compressible viscous flows, originally proposed in Xu et al. [39], for the simulation of commercial aircraft applications. The methodology, which is based on the Navier–Stokes equations of compressible flows in an arbitrary Lagrangian–Eulerian (ALE) frame, is formulated using pressure-primitive variables and the reduced-energy equation to facilitate FSI modeling. The framework is comprised of the SUPG stabilization, the weakly enforced essential boundary conditions, and a discontinuity-capturing operator for conservation variables. This paper presents a summary of the formulations and introduces a new entropy-based shock-capturing operator [28] that allows us to obtain better solutions for the class of problems considered in this work. The accuracy and robustness of the framework is tested for various Mach numbers ranging from low-subsonic to transonic flow regimes. The aerodynamic simulations are carried out for two dimensional (2D) validation cases of flow around the NACA 0012 [56–58] and RAE 2822 [59] airfoils and three dimensional (3D) cases of flow over the ONERA M6 wing [60] and the NASA Common Research Model (CRM) aircraft [61–63]. The simulation results of all cases are compared with the corresponding experimental data to demonstrate the accuracy and effectiveness of the present framework for the prediction of aircraft aerodynamics.

This paper is outlined as follows. First, we introduce the variational form of the SUPG-based Navier–Stokes equations of compressible flow in pressure-primitive variables along with weakly enforced essential boundary conditions and the entropy-based shock-capturing definition. Later, we present the 2D simulation results of flow over the NACA 0012 and RAE 2822 airfoils at different flow conditions. We also apply the method to simulate 3D flow over the ONERA M6 wing model and the NASA CRM wing-body model and compare all the simulation results with the corresponding experimental or computational data. Finally, we draw conclusions on the accuracy of the results obtained using the present methodology for aerospace applications.

2 Methodology

This section summarizes the finite-element-based variational formulation for the Navier–Stokes equations of compressible flows in an ALE frame [39]. The formulation is stabilized using the SUPG stabilization methodology and is augmented with a discontinuity-capturing operator and weak enforcement of essential boundary conditions. Throughout the paper, $(\cdot)_{,t}$ denotes a partial time derivative taken with respect to a fixed spatial coordinate in the referential domain, and $(\cdot)_{,i}$ denotes a spatial gradient, where $i = 1, \ldots, d$ for a spatial domain of dimension d. The convention used for i applies to j and k. The Einstein summation convention on repeated indices is also used throughout.

2.1 Strong form

The Navier–Stokes equations of compressible flows with a reduced form of the energy equations [39,47] are considered as the governing equations in this work. Before writing the formulation in the ALE frame, we first introduce a reduced-conservation-variable vector, $\mathbf{U}$, and a pressure-primitive-variable vector, $\mathbf{Y}$, as

$$\mathbf{U} = \begin{bmatrix} \rho \\ \rho u_1 \\ \rho u_2 \\ \rho u_3 \\ \rho e \end{bmatrix}, \qquad \mathbf{Y} = \begin{bmatrix} p \\ u_1 \\ u_2 \\ u_3 \\ T \end{bmatrix}, \tag{1}$$

where ρ is the density, u_i is the ith velocity component, e is the fluid internal energy density, p is the pressure, and T is the temperature. Pressure, density, and temperature are related through the ideal gas equation of state, $p = \rho RT$, where R is the ideal gas constant. Furthermore, we assume a calorically perfect gas and define the fluid internal energy density as $e = c_v T$, where $c_v = R/(\gamma - 1)$ is the specific heat at constant volume, and γ is the heat capacity ratio.

Remark 1 $\mathbf{U}$ was designated as the vector of *reduced* conservation variables since it was derived from the conservation-variable vector $\tilde{\mathbf{U}}$ for the reduced form of the energy equation (see Xu et al. [39, Section 2.1] for details).

The convective ALE formulation of the balance of mass, linear momentum, and energy in quasi-linear form involving $\mathbf{U}$ may be stated as

$$\mathbf{U}_{,t} + \hat{\mathbf{A}}_i^{\mathrm{ALE}} \mathbf{U}_{,i} - \left(\hat{\mathbf{K}}_{ij} \mathbf{U}_{,j}\right)_{,i} - \mathbf{S} = \mathbf{0}, \tag{2}$$

where $\hat{\mathbf{A}}_i^{\mathrm{ALE}} = \hat{\mathbf{A}}_i + \hat{\mathbf{A}}_i^{\mathrm{sp}} - \hat{u}_i \mathbf{I}$, $\hat{\mathbf{A}}_i = \frac{\partial \mathbf{F}_i^{\mathrm{adv}}}{\partial \mathbf{U}}$, $\hat{\mathbf{A}}_i^{\mathrm{sp}}$ is such that $\hat{\mathbf{A}}_i^{\mathrm{sp}} \mathbf{U}_{,i} = \mathbf{F}^{\mathrm{sp}}$, $\mathbf{I}$ is a 5×5 identity matrix, $\hat{u}_i$ is the ith component of the fluid domain velocity $\hat{\mathbf{u}}$, $\hat{\mathbf{K}}_{ij}$ is such that $\hat{\mathbf{K}}_{ij} \mathbf{U}_{,j} = \mathbf{F}_i^{\mathrm{diff}}$, $\mathbf{F}_i^{\mathrm{adv}}$ and $\mathbf{F}_i^{\mathrm{diff}}$ are the vectors of convective and diffusive fluxes, respectively, defined as

$$\mathbf{F}_i^{\mathrm{adv}} = \mathbf{F}_i^{\mathrm{adv}\backslash p} + \mathbf{F}_i^{p} = \begin{bmatrix} \rho u_i \\ \rho u_i u_1 \\ \rho u_i u_2 \\ \rho u_i u_3 \\ \rho u_i e \end{bmatrix} + \begin{bmatrix} 0 \\ p\delta_{1i} \\ p\delta_{2i} \\ p\delta_{3i} \\ 0 \end{bmatrix} \tag{3}$$

and

$$\mathbf{F}_i^{\mathrm{diff}} = \begin{bmatrix} 0 \\ \tau_{1i} \\ \tau_{2i} \\ \tau_{3i} \\ -\phi_i^q \end{bmatrix}, \tag{4}$$

$\mathbf{F}^{\mathrm{sp}}$ is the contribution of stress–power in the energy equation, defined as

$$\mathbf{F}^{\mathrm{sp}} = \begin{bmatrix} 0 \\ 0 \\ 0 \\ 0 \\ p u_{i,i} - \tau_{ij} u_{j,i} \end{bmatrix}, \tag{5}$$

and $\mathbf{S}$ is the source term. In Eqs. (3)–(5), δ_{ij} is the Kronecker delta, and τ_{ij} and ϕ_i^q are the viscous stress and heat flux, respectively, given by $\tau_{ij} = \lambda u_{k,k} \delta_{ij} + \mu \left(u_{i,j} + u_{j,i}\right)$ and $\phi_i^q = -\kappa T_{,i}$, where μ is the dynamic viscosity, λ is the second coefficient of viscosity ($\lambda = -2\mu/3$ based on Stokes' hypothesis), and κ is the thermal conductivity.

Analogously, in the case of pressure-primitive variables $\mathbf{Y}$, the quasi-linear form of Eq. (2) can be written as

$$\mathbf{A}_0 \mathbf{Y}_{,t} + \mathbf{A}_i^{\mathrm{ALE}} \mathbf{Y}_{,i} - \left(\mathbf{K}_{ij} \mathbf{Y}_{,j}\right)_{,i} - \mathbf{S} = \mathbf{0}, \tag{6}$$

where $\mathbf{A}_i^{\mathrm{ALE}} = \mathbf{A}_i + \mathbf{A}_i^{\mathrm{sp}} - \hat{u}_i \mathbf{A}_0$, $\mathbf{A}_0 = \frac{\partial \mathbf{U}}{\partial \mathbf{Y}}$, $\mathbf{A}_i = \frac{\partial \mathbf{F}_i^{\mathrm{adv}}}{\partial \mathbf{Y}} = \hat{\mathbf{A}}_i \mathbf{A}_0$, $\mathbf{A}_i^{\mathrm{sp}}$ is such that $\mathbf{A}_i^{\mathrm{sp}} \mathbf{Y}_{,i} = \mathbf{F}^{\mathrm{sp}}$, and $\mathbf{K}_{ij}$ is such that $\mathbf{K}_{ij} \mathbf{Y}_{,j} = \mathbf{F}_i^{\mathrm{diff}}$. Based on the splitting of $\mathbf{F}_i^{\mathrm{adv}}$ into $\mathbf{F}_i^{\mathrm{adv}\backslash p}$ and $\mathbf{F}_i^{p}$, we can further split $\mathbf{A}_i$ as $\mathbf{A}_i = \mathbf{A}_i^{\mathrm{adv}\backslash p} + \mathbf{A}_i^{p}$ to separate the pressure term from the convective flux. Detailed expressions for the matrices appearing in the quasi-linear forms can be found in Xu et al. [39, Appendix A].

It should be noted that the choice of conservation or pressure-primitive variables does not change the balance laws. In the present work, we use pressure-primitive variables because, unlike for conservation variables, the incompressible limit of the Euler-Jacobian matrices is well defined for the pressure-primitive variables [28]. In addition, as will be seen in the next section, the weak boundary condition operator for the pressure-primitive variables becomes a simple extension of the incompressible-flow case.

Finally, for the developments in the next section, we define the strong-form residual of the Navier–Stokes partial differential equations as

$$\mathbf{Res}\,(\mathbf{Y}) = \mathbf{A}_0 \mathbf{Y}_{,t} + \mathbf{A}_i^{\mathrm{ALE}} \mathbf{Y}_{,i} - \left(\mathbf{K}_{ij} \mathbf{Y}_{,j}\right)_{,i} - \mathbf{S}. \tag{7}$$

Note that if $\mathbf{Y}$ is the exact analytical solution of the Navier–Stokes equations, then $\mathbf{Res}\,(\mathbf{Y}) = \mathbf{0}$.

2.2 Weak form

The weak form of the Navier–Stokes equations of compressible flows stated in the previous section can be written as follows. Let $\Omega \in \mathbb{R}^d$ denote the spatial domain and Γ be its boundary. Assume the fluid domain Ω is divided into N_{el} spatial finite elements each denoted by Ω^e and the fluid domain boundary Γ is decomposed into N_{eb} surface elements where the bth element is denoted by Γ^b. Let $\mathcal{S}^h$ be the discrete trial function space for the pressure-primitive variables and $\mathcal{V}^h$ be the discrete test function space for the compressible-flow equation system, both defined over Ω. Let the essential boundary conditions be enforced on $\Gamma_{\mathrm{D}} \in \Gamma$. The semi-discrete weak form of the compressible-flow problem may be stated as: Find $\mathbf{Y}^h = [p^h \ \mathbf{u}^h \ T^h]^{\mathrm{T}} \in \mathcal{S}^h$ such that for all test functions $\mathbf{W}^h = [q^h \ \mathbf{w}^h \ w_\theta^h]^{\mathrm{T}} \in \mathcal{V}^h$,

$$B\left(\mathbf{W}^h, \mathbf{Y}^h\right) - F\left(\mathbf{W}^h\right) + B^{\mathrm{DC}}\left(\mathbf{W}^h, \mathbf{Y}^h\right) - \sum_{b=1}^{N_{eb}} \int_{\Gamma^b \cap \Gamma_{\mathrm{D}}} \mathbf{w}^h \cdot \left(\boldsymbol{\sigma}(\mathbf{u}^h, p^h)\mathbf{n}\right) \mathrm{d}\Gamma$$

$$
\begin{aligned}
&- \sum_{b=1}^{N_{eb}} \int_{\Gamma^b \cap \Gamma_{\mathrm{D}}} \left(\delta\boldsymbol{\sigma}(\mathbf{w}^h, q^h)\mathbf{n} \right) \cdot \left(\mathbf{u}^h - \mathbf{g}^h \right) \, \mathrm{d}\Gamma \\
&- \sum_{b=1}^{N_{eb}} \int_{\Gamma^b \cap \Gamma_{\mathrm{D}}^-} \mathbf{w}^h \cdot \rho \left(\left(\mathbf{u}^h - \hat{\mathbf{u}}^h \right) \cdot \mathbf{n} \right) \left(\mathbf{u}^h - \mathbf{g}^h \right) \, \mathrm{d}\Gamma \\
&+ \sum_{b=1}^{N_{eb}} \int_{\Gamma^b \cap \Gamma_{\mathrm{D}}} \mathbf{w}^h \cdot \tau_\mu \left(\mathbf{u}^h - \mathbf{g}^h \right) \, \mathrm{d}\Gamma \\
&+ \sum_{b=1}^{N_{eb}} \int_{\Gamma^b \cap \Gamma_{\mathrm{D}}} \left(\mathbf{w}^h \cdot \mathbf{n} \right) \tau_\lambda \left(\left(\mathbf{u}^h - \mathbf{g}^h \right) \cdot \mathbf{n} \right) \, \mathrm{d}\Gamma \\
&- \sum_{b=1}^{N_{eb}} \int_{\Gamma^b \cap \Gamma_{\mathrm{D}}} w_\theta^h \kappa \nabla T^h \cdot \mathbf{n} \, \mathrm{d}\Gamma \\
&- \sum_{b=1}^{N_{eb}} \int_{\Gamma^b \cap \Gamma_{\mathrm{D}}} \kappa \nabla w_\theta^h \cdot \mathbf{n} \left(T^h - T_{\mathrm{B}} \right) \, \mathrm{d}\Gamma \\
&- \sum_{b=1}^{N_{eb}} \int_{\Gamma^b \cap \Gamma_{\mathrm{D}}^-} w_\theta^h \rho c_{\mathrm{v}} \left(\left(\mathbf{u}^h - \hat{\mathbf{u}}^h \right) \cdot \mathbf{n} \right) \left(T^h - T_{\mathrm{B}} \right) \, \mathrm{d}\Gamma \\
&+ \sum_{b=1}^{N_{eb}} \int_{\Gamma^b \cap \Gamma_{\mathrm{D}}} w_\theta^h \tau_\kappa \left(T^h - T_{\mathrm{B}} \right) \, \mathrm{d}\Gamma = 0 \, . \qquad (8)
\end{aligned}
$$

Here, $\mathbf{g}^h$ is the prescribed velocity on the no-slip boundary, T_{B} is the prescribed temperature on the boundary, $\mathbf{n}$ is the unit outward normal vector to the fluid domain, Γ_{D}^- is the inflow part of Γ_{D} where $(\mathbf{u}^h - \hat{\mathbf{u}}^h) \cdot \mathbf{n} < 0$, and $\boldsymbol{\sigma}$ and $\delta\boldsymbol{\sigma}$ are the stress tensor and its variation, respectively, defined as

$$
\begin{aligned}
\boldsymbol{\sigma}(\mathbf{u}^h, p^h) = &-p^h \mathbf{I} + \left(\lambda \nabla \cdot \mathbf{u}^h \right) \mathbf{I} \\
&+ \mu \left(\nabla \mathbf{u}^h + (\nabla \mathbf{u}^h)^{\mathrm{T}} \right) \qquad (9)
\end{aligned}
$$

and

$$
\begin{aligned}
\delta\boldsymbol{\sigma}(\mathbf{w}^h, q^h) = &\rho q^h \mathbf{I} + \left(\lambda \nabla \cdot \mathbf{w}^h \right) \mathbf{I} \\
&+ \mu \left(\nabla \mathbf{w}^h + (\nabla \mathbf{w}^h)^{\mathrm{T}} \right) . \qquad (10)
\end{aligned}
$$

The first two terms in Eq. (8) are given by

$$
\begin{aligned}
&B\left(\mathbf{W}^h, \mathbf{Y}^h \right) \\
&= \int_\Omega \mathbf{W}^h \cdot \left(\mathbf{A}_0 \mathbf{Y}_{,t}^h + \mathbf{A}_i^{\mathrm{adv}\backslash \mathrm{p}} \mathbf{Y}_{,i}^h + \mathbf{A}_i^{\mathrm{sp}} \mathbf{Y}_{,i}^h \right) \, \mathrm{d}\Omega \\
&\quad - \int_\Omega \mathbf{W}_{,i}^h \cdot \left(\mathbf{A}_i^p \mathbf{Y}^h - \mathbf{K}_{ij} \mathbf{Y}_{,j}^h \right) \, \mathrm{d}\Omega \\
&\quad + \sum_{e=1}^{N_{el}} \int_{\Omega^e} \left(\left(\mathbf{A}_i^{\mathrm{ALE}} \right)^{\mathrm{T}} \mathbf{W}_{,i}^h \right) \cdot \left(\mathbf{A}_0^{-1} \hat{\boldsymbol{\tau}}_{\mathrm{SUPG}} \right) \mathbf{Res}(\mathbf{Y}^h) \, \mathrm{d}\Omega \\
&\qquad (11)
\end{aligned}
$$

and

$$
F\left(\mathbf{W}^h \right) = \int_\Omega \mathbf{W}^h \cdot \mathbf{S}^h \, d\Omega + \int_{\Gamma_{\mathbf{H}}} \mathbf{W}^h \cdot \mathbf{H}^h \, d\Gamma, \qquad (12)
$$

where $\mathbf{A}_0^{-1} = \frac{\partial \mathbf{Y}^h}{\partial \mathbf{U}^h}$. On the right-hand side of Eq. (11), the first two terms correspond to the Galerkin form of the Navier–Stokes equations of compressible flows, and the third term is the SUPG stabilization [10–23]. $\hat{\boldsymbol{\tau}}_{\mathrm{SUPG}}$ is the stabilization matrix, and we refer the reader to Xu et al. [39] for more details. In Eq. (12), the vector $\mathbf{H}^h$ contains the prescribed values of the fluid traction and heat flux boundary conditions.

The third term in Eq. (8) is the discontinuity-capturing (DC) operator [24–35], which, in the present work, is defined as

$$
B^{\mathrm{DC}}\left(\mathbf{W}^h, \mathbf{Y}^h \right) = \sum_{e=1}^{N_{el}} \int_{\Omega^e} \mathbf{W}_{,i}^h \cdot \left(\hat{\kappa}^{\mathrm{DC}} \mathbf{A}_0 \right) \mathbf{Y}_{,i}^h \, \Omega \, , \qquad (13)
$$

where $\hat{\kappa}^{\mathrm{DC}}$ is the scalar artificial viscosity given by

$$
\hat{\kappa}^{\mathrm{DC}} = C \left(\frac{\mathbf{Res}(\mathbf{Y}^h)^{\mathrm{T}} \tilde{\mathbf{A}}_0^{-1} \mathbf{Res}(\mathbf{Y}^h)}{G_{ij} \mathbf{U}_{,i}^{h\,\mathrm{T}} \tilde{\mathbf{A}}_0^{-1} \mathbf{U}_{,j}^h} \right)^{\frac{1}{2}} . \qquad (14)
$$

In the above, C is a $\mathcal{O}(1)$ positive constant, $G_{ij} = \xi_{k,i} \, \xi_{k,j}$ is the element metric tensor derived from the element geometric mapping from the parent to physical coordinates $\mathbf{x}(\boldsymbol{\xi})$, and $\tilde{\mathbf{A}}_0$ is the zeroth Euler–Jacobian of the transformation between the conservation and entropy variables (see Hauke and Hughes [28, Eq. A.82]). To avoid division by zero, a small positive number is introduced in the denominator in addition to the solution-dependent terms. Equation (14) is an extension of the δ_{91} definition designed by Le Beau, Tezduyar and colleagues [11,64], where only the convective part of the full residual operator $\mathbf{Res}(\mathbf{Y}^h)$ was employed. While the SUPG terms provide the necessary stability across a wide range of Reynolds numbers, the discontinuity-capturing operator provides the necessary additional dissipation in the shock regions. Note that both SUPG stabilization and discontinuity-capturing operators are homogeneous functions of the strong residual of the Navier–Stokes equations (see Eq. (7)), which renders the resulting method consistent and provides a pathway to higher-order accuracy.

Remark 2 The definition of $\hat{\kappa}^{\mathrm{DC}}$ in Eqs. (13) and (14) is based on the physical-coordinate derivatives. This produces a definition of the shock viscosity that is isotropic for the conservation variables, which, in turn, guarantees objectivity.

In Eq. (8), the terms from the second line to the last line correspond to the weak enforcement of the velocity and temperature boundary conditions. Weak imposition of essential

boundary conditions was first introduced in Bazilevs et al. [36–38] for incompressible flows and later extended to compressible flows in Xu et al. [39]. Imposing the Dirichlet boundary conditions weakly allows a certain amount of flow to slip on the solid surface, which removes some of the burden from the boundary-layer mesh to resolve the sharp velocity gradients near the wall. This effect imitates the presence of a boundary layer that would otherwise need to be resolved with spatial refinement, allowing more accurate solutions on coarse boundary-layer meshes [39–43]. We refer the reader to Xu et al. [39] for the detailed definitions of the penalty parameters τ_μ, τ_λ, and τ_κ in Eq. (8). Note that for problems with adiabatic boundary conditions, the terms on the last two lines of Eq. (8) are removed.

In the last two decades, the research on variational multiscale (VMS) methods was able to explain the origins of stabilized methods [65] and to connect stabilization operators with the subgrid-scale models of turbulence [66]. In particular, the SUPG formulation may be viewed as a residual-based VMS (RBVMS) model of turbulence with an algebraic closure model for the unresolved subgrid scales [67]. For incompressible flows, RBVMS was shown to perform best in the regime of large-eddy simulation (LES) [68] modeling of turbulent flows [69–85]. Just like traditional LES, RBVMS alone requires relatively fine boundary-layer resolution to deliver accurate results for wall-bounded turbulent flows. Weak enforcement of the no-slip conditions at the wall in the context of RBVMS significantly reduces the boundary-layer resolution requirements while maintaining good accuracy of large scales in the flow [36–43]. Although weak no-slip boundary condition enforcement is unique to the variational methods (i.e., to the best of the authors knowledge, there is no equivalent formulation in finite-difference or finite-volume approaches), its ability to preserve good solution accuracy on relatively coarse boundary-layer meshes is akin to that of near-wall modeling approaches in traditional CFD [86], as investigated in Bazilevs et al. [37] and Golshan et al. [44]. As such, the computational methodology presented in this work may be classified as LES with near-wall modeling.

The semi-discrete weak form of the compressible-flow equations given by Eq. (8) is discretized in time using a second-order accurate, implicit generalized-α method [87–89]. The solution of the nonlinear algebraic equation system resulting from the generalized-α scheme is obtained at each time step using the Newton–Raphson method. GMRES with block-diagonal preconditioning [90] is used to approximately solve the linear equation system at each Newton–Raphson iteration.

Remark 3 The formulations presented here are all developed in the ALE frame suitable for moving-domain simulations. While the numerical examples in this work are all considered in fixed domains, the ALE version of the formulation is presented here for completeness. For computations with a fixed fluid domain, one can simply set $\hat{\mathbf{u}} = \mathbf{0}$ in the above equations.

3 Results and discussions

This section presents and validates the CFD results obtained using finite-element-based compressible flow Navier-Stokes equations augmented with SUPG stabilization, DC operator, and weakly enforced essential boundary conditions. We report the simulation results for flow around the NACA 0012 airfoil, RAE 2822 supercritical airfoil, ONERA M6 wing, and NASA CRM wing-body aircraft. The simulated flow problems cover Reynolds and Mach numbers ranging from low-subsonic to transonic regimes, illustrating the general applicability of the compressible-flow formulation presented in this work.

3.1 Flow over the NACA 0012 Airfoil

Case 1: The first validation example is the simulation of flow over the 2D NACA 0012 airfoil from the NASA Turbulence Modeling Resource [91], which is one of the fundamental benchmark cases for code validation. Ladson [56] and Gregory and O'Reilly [57] conducted several experimental tests of flow over the NACA 0012 airfoil at different flow conditions and documented the pressure distributions over the airfoil. The freestream flow conditions for the first selected case are $M = 0.15$, $Re = 6 \times 10^6$, $T = 300K$, and $\alpha = 10°$. The selected case is run and tested on meshes provided by the NASA Turbulence Modeling Resource [91].

Three structured meshes with 225×65, 449×129, and 897×257 elements are selected and labeled as coarse, medium, and fine grids, respectively. The grids have a farfield boundary at $500c$, where $c = 1$ is the chord length for the selected NACA 0012 airfoil. Figure 1a shows the near-airfoil discretization for the medium grid case. On the airfoil surface, no-slip velocity boundary conditions are enforced weakly in the tangential components, and a strong zero velocity (no-penetration) boundary condition is imposed in the normal surface component. Additionally, the airfoil surface is assumed to be adiabatic with a zero heat-flux boundary condition. The temperature-dependent viscosity value is set according to Sutherland's law as

$$\mu = \mu_r \left(\frac{T}{T_r}\right)^{3/2} \frac{T_r + S}{T + S}, \tag{15}$$

and the thermal conductivity is calculated using

$$\kappa = \mu c_p / Pr, \tag{16}$$

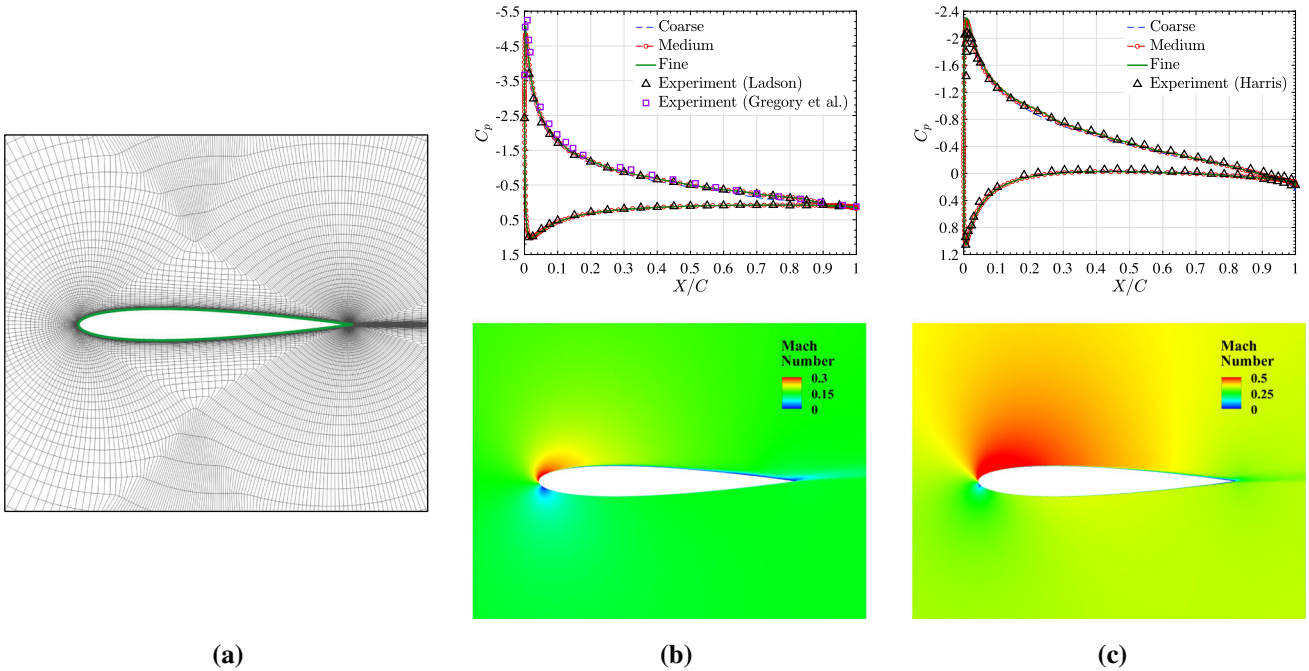

Fig. 1 (**a**) Near-airfoil mesh discretization of the NACA 0012 airfoil for the medium grid case (449 × 129 elements). (**b**) Pressure coefficient comparison plot for different grid sizes compared with experimental data [56,57] (top) and Mach number contour plot (bottom) for Case 1: $M = 0.15$, $Re = 6$ million, $\alpha = 10°$. (**c**) Pressure coefficient plot for different grid sizes compared with experimental data [58] (top) and Mach number contour plot (bottom) for Case 2: $M = 0.35$, $Re = 3$ million, $\alpha = 5.88°$

where $\mu_r = 1.716 \times 10^{-5}$ kg/(m·s), $T_r = 273.15$ K, $S = 110.4$ K, $Pr = 0.72$, and c_p is the specific heat at constant pressure calculated based on $\gamma = 1.4$.

Figure 1b (bottom) shows the Mach number contour plot for the simulation performed using the medium grid case. Figure 1b (top) shows the pressure coefficient (C_p) plot along the airfoil location from the leading edge ($X/C = 0$) to trailing edge ($X/C = 1$). The plot shows the mesh convergence study performed on all three grids compared with the two experimental data sets [56,57]. The results obtained from the CFD simulations show solution convergence under mesh refinement and demonstrate good agreement with the experimental data.

Case 2: Another case of flow over the NACA 0012 airfoil is computed for a low-subsonic compressible flow regime. The freestream flow conditions for the selected case are $M = 0.35$, $Re = 3 \times 10^6$, $T = 300K$, and $\alpha = 5.88°$. The experimental testing at the selected flow condition has been well studied, and documentation of the pressure coefficient results can be found in Harris [58]. The same three structured grids from case 1 are used to perform the simulations at the given flow condition in case 2. On the airfoil surface, no-slip velocity boundary conditions are enforced weakly in the tangential components, and a strong zero velocity (no-penetration) boundary condition is imposed in the normal surface component. Additionally, the airfoil surface is assumed to be adiabatic with a zero heat-flux boundary condition. The temperature-dependent viscosity and thermal conductivity values are determined according to Eqs. (15) and (16) with $\mu_r = 1.716 \times 10^{-5}$ kg/(m·s), $T_r = 273.15$ K, $S = 110.4$ K, $Pr = 0.72$, and c_p the specific heat at constant pressure calculated based on $\gamma = 1.4$.

Figure 1c (bottom) shows the 2D Mach number contour plot around the airfoil for the simulation performed using the medium grid case. Figure 1c (top) shows the pressure coefficient (C_p) plot along the airfoil location from the leading edge ($X/C = 0$) to trailing edge ($X/C = 1$). The plot shows the mesh convergence study performed on all three grids compared with the two experimental data sets from Harris [58]. The CFD results demonstrate convergence under mesh refinement and good agreement with the experimental results.

3.2 Transonic flow over the RAE 2822 Airfoil

The present methodology is also applied to simulate flow over the RAE 2822 airfoil in the transonic flow regime. The selected test case has been experimentally well studied and documented by Cook et al. [59]. Transonic flow over the RAE 2822 is one of the standard cases for compressible flow validation studies because of the strong shock wave formation on the upper surface of the airfoil, which can induce boundary-layer separation. The free-stream flow conditions for the selected case are $M = 0.728$, $Re = 6.5 \times 10^6$,

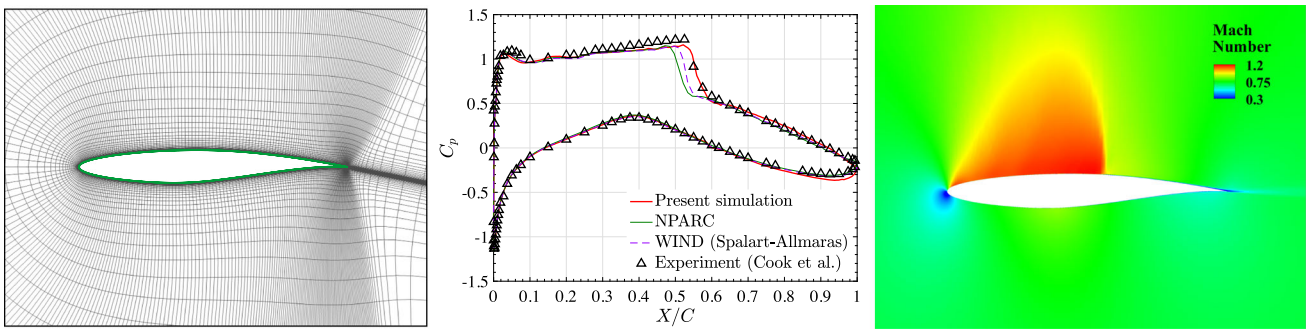

Fig. 2 (**a**) Near-airfoil mesh discretization of the RAE 2822 airfoil. (**b**) Pressure coefficient plot compared with the experimental data [59] and simulated results from the WIND code [92]. (**c**) Mach number contour plot around the RAE 2822 airfoil: $M = 0.729$, $Re = 6.5$ million, $\alpha = 2.31°$

$T = 255.556$ K, and $\alpha = 2.31°$. The standard mesh of size 395×65 with 306 points on the airfoil surface provided by the NPARC Alliance Verification and Validation Archive [93] was used to obtain a direct comparison with the other simulated data. Figure 2a shows the near-airfoil discretization for the selected grid. On the airfoil surface, no-slip velocity boundary conditions are enforced weakly in the tangential components, and a strong zero velocity (no-penetration) boundary condition is imposed in the normal surface component. A zero heat-flux temperature boundary condition is also applied on the airfoil surface. The temperature-dependent viscosity and thermal conductivity values are determined according to Eqs. (15) and (16) with $\mu_r = 1.716 \times 10^{-5}$ kg/(m·s), $T_r = 273.15$ K, $S = 110.4$ K, $Pr = 0.72$, and c_p the specific heat at constant pressure calculated based on $\gamma = 1.4$.

The simulated flow field around the RAE 2822 airfoil was examined through the Mach number contour field and pressure coefficient C_p data plotted along the airfoil. Figure 2c shows the Mach number contour plot, which clearly shows the smooth formation of the shock on the upper surface of the airfoil. Figure 2b shows the pressure coefficient results compared with the experimental data set from Cook et al. [59] and the simulated results from the WIND code provided by the NPARC Alliance Verification and Validation Archive [92]. The results for the pressure coefficient data obtained from the present simulations show good agreement with the experimental results. In particular, the shock location and the drop in the pressure is accurately captured in the simulation, which demonstrates the effectiveness of the entropy-based discontinuity-capturing operator used in the present finite-element framework.

3.3 ONERA M6 Wing

The simulation of flow over the 3D ONERA M6 wing is performed in the transonic flow regime. The selected test case has been experimentally studied, and the pressure coefficient results have been well documented by documented by Schmitt and Charpin [60] as ONERA M6 case number 2308. The free-stream flow conditions for the selected case are $M = 0.84$, $Re = 14.6 \times 10^6$ based on the root chord, $T = 300$ K, and $\alpha = 3.06°$. At these conditions, the simple geometry of the ONERA M6 wing features complex flow phenomenon, such as boundary-layer interaction and flow separation, and the experimental results have been widely used for CFD validation studies. Figure 3 shows the ONERA M6 experimental setup and corresponding CAD geometry, obtained from the NASA Turbulence Modeling Resource [94] and NPARC Alliance Verification and Validation Archive [95], together with the computational domain and boundary conditions. Fig. 4 shows the unstructured mesh of the computational domain and two additional enlarged views of the mesh near the wing. On the surface of the wing, the no-slip boundary conditions are enforced weakly, while the no-penetration boundary conditions are imposed strongly. A zero heat-flux temperature boundary condition is also applied on the airfoil surface. Symmetry boundary conditions are imposed on the plane extending from the wing root. The temperature-dependent viscosity and thermal conductivity values are determined according to Eqs. (15) and (16) with $\mu_r = 1.716 \times 10^{-5}$ kg/(m·s), $T_r = 273.15$ K, $S = 110.4$ K, $Pr = 0.72$, and c_p the specific heat at constant pressure calculated based on $\gamma = 1.4$.

To show the solution convergence, a refinement study based on three different meshes was carried out. The mesh statistics are summarized in Table 1. Figure 5 shows the results for the pressure coefficient at different spanwise locations, which demonstrates the solution convergence under mesh refinement. Figure 6 shows the pressure coefficient contour plot on the surface of the ONERA M6 wing, which clearly demonstrates the smooth formation and capturing of the shock structures on the wing. The pressure coefficient (C_p) data at different spanwise locations (η) on the wing for the medium level mesh are also compared with the experimental data set [60] and the simulated results from the

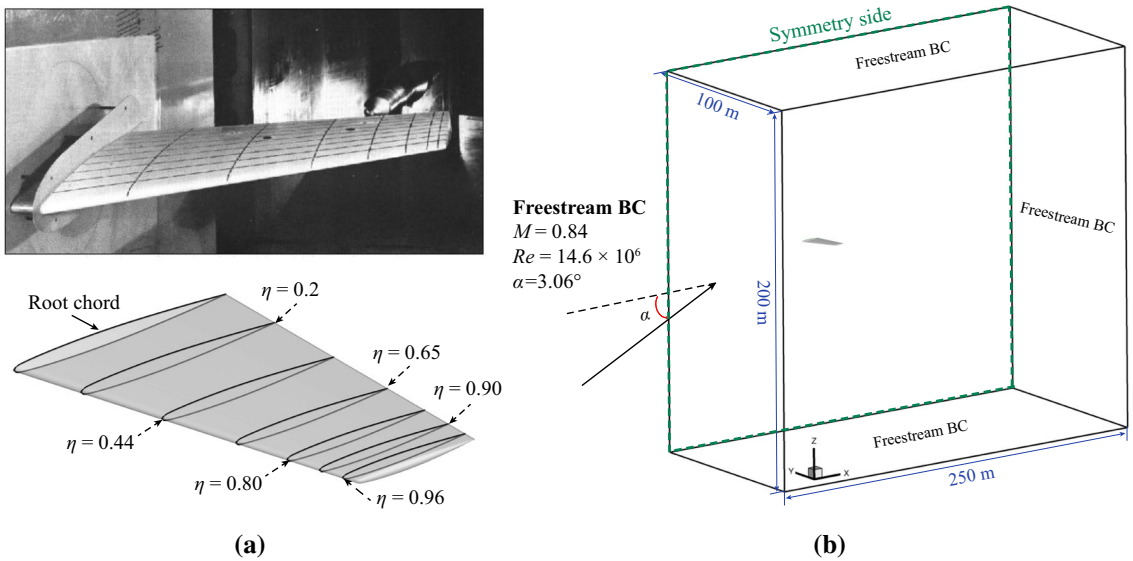

Fig. 3 (**a**) ONERA M6 experimental wind-tunnel setup [60] and CAD geometry model showing different spanwise locations. (**b**) Computational domain and boundary conditions

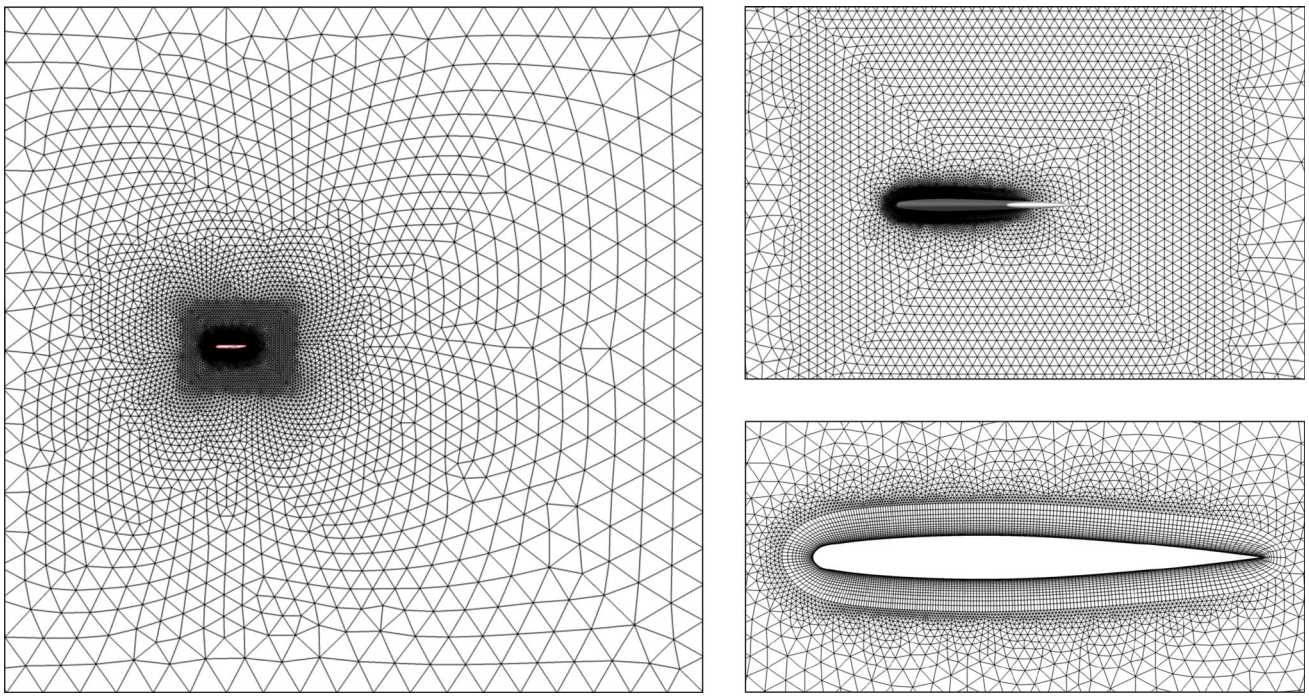

Fig. 4 Computational mesh and near-surface mesh discretization for the ONERA M6 case

FUN3D (SA-neg) [96] and WIND [97] codes, as shown in Fig. 7. The results for the pressure coefficient data obtained from the present simulations are in good agreement with the experimental results. Additionally, in the present simulation, the spacing of the first boundary-layer element height normal to the wing surface for the medium level mesh is 0.001 m, which is approximately 60 times larger than the mesh used to obtain results from FUN3D and WIND codes. The results obtained using the coarser boundary-layer mesh demonstrate the effectiveness of the weakly enforced essential boundary conditions in capturing accurate near-wall solutions without high boundary-layer resolution requirements. The accuracy in capturing the shock locations and pressure drops at different spanwise locations on the wing shows the effectiveness of the entropy-based discontinuity-capturing operator for three dimensional flow problems.

Table 1 ONERA M6 mesh statistics for refinement study

Mesh	Total number of elements	Element size on wing surface (m)	Number of boundary layers	First boundary layer height (m)	Growth ratio	Outer domain element size (m)
Coarse	1,296,546	0.02	9	0.002	1.2	25
Medium	5,317,478	0.01	12	0.001	1.2	12.5
Fine	13,558,505	0.005	15	0.0005	1.2	6.25

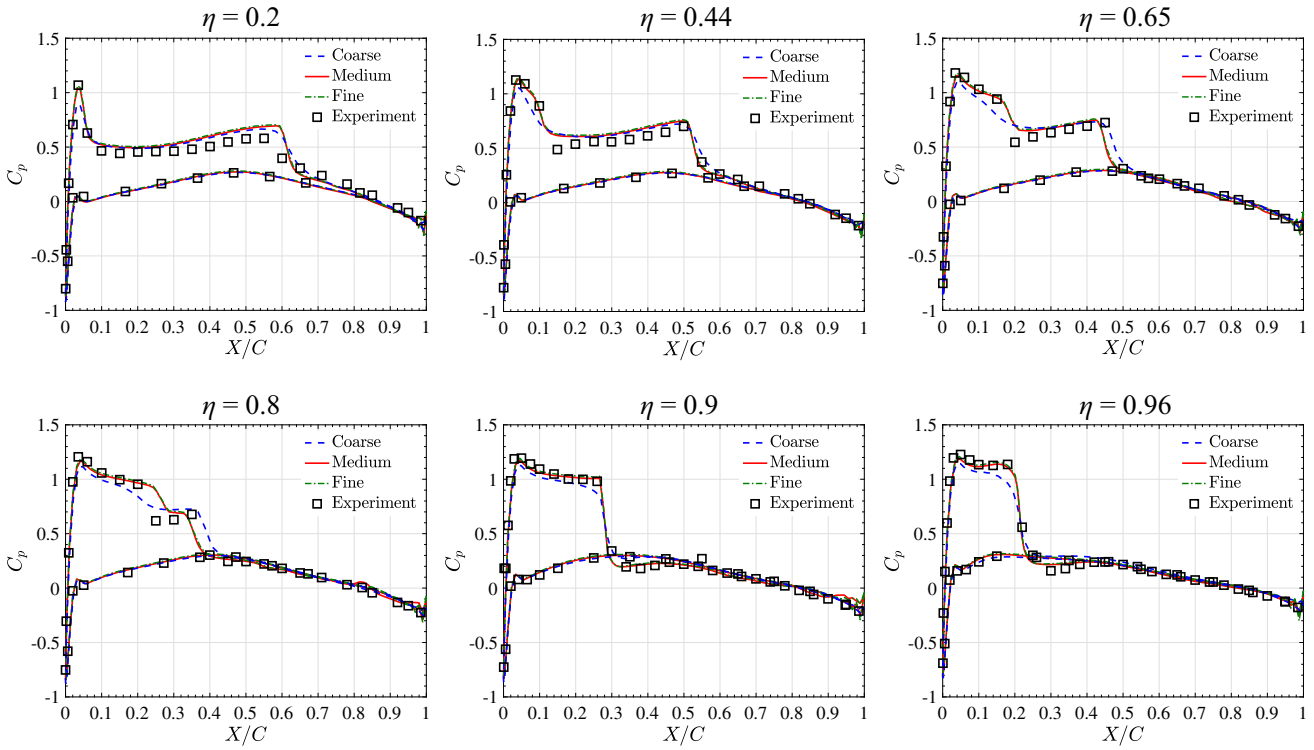

Fig. 5 Pressure coefficient plot for different ONERA M6 mesh sizes compared with experimental data [60]. See Fig. 3 for corresponding η locations

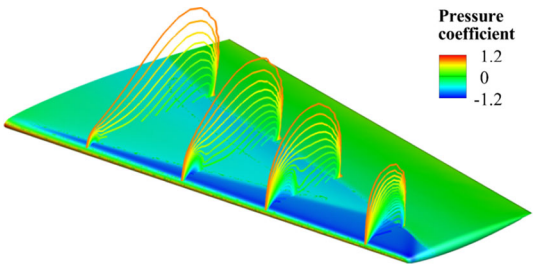

Fig. 6 Pressure coefficient contour plot on the ONERA M6 wing surface. Line contour of the pressure slices are also plotted at different wing locations to illustrate the shock formation

3.4 Common Research Model

3D flow simulation over the NASA CRM wing-body configuration is performed at transonic conditions [61]. The CRM geometry and simulation conditions mimic the design of a modern commercial aircraft and were initially designed for the benchmark problem in the 6th AIAA CFD Drag Prediction Workshop [98]. Experimental studies of the NASA CRM have been conducted in the NASA Langley National Transonic Facility (NTF) and the NASA Ames 11-Foot Transonic Wind Tunnel (11-ft TWT), and the experimental pressure coefficient results are well documented [62,63]. Experimental investigations have been performed at different Reynolds numbers and CRM configurations with optional horizontal tail and optional nacelle/pylon attached to the model. In this study, we consider and simulate the half-cut model of the wing-body (without horizontal tail and nacelle/pylon) configuration using free-stream flow conditions of $M = 0.85$, $Re = 5 \times 10^6$ based on the mean aerodynamic chord, $T = 310.9$ K, and $\alpha = 2.75°$. Figure 8 shows the experimental setup and CAD geometry of the CRM wing-body and the computational domain along with the domain boundary conditions. The CRM wing-body geometry considered in this simulation corresponds to the 2.75-degree aeroelastic deflection geometry model obtained

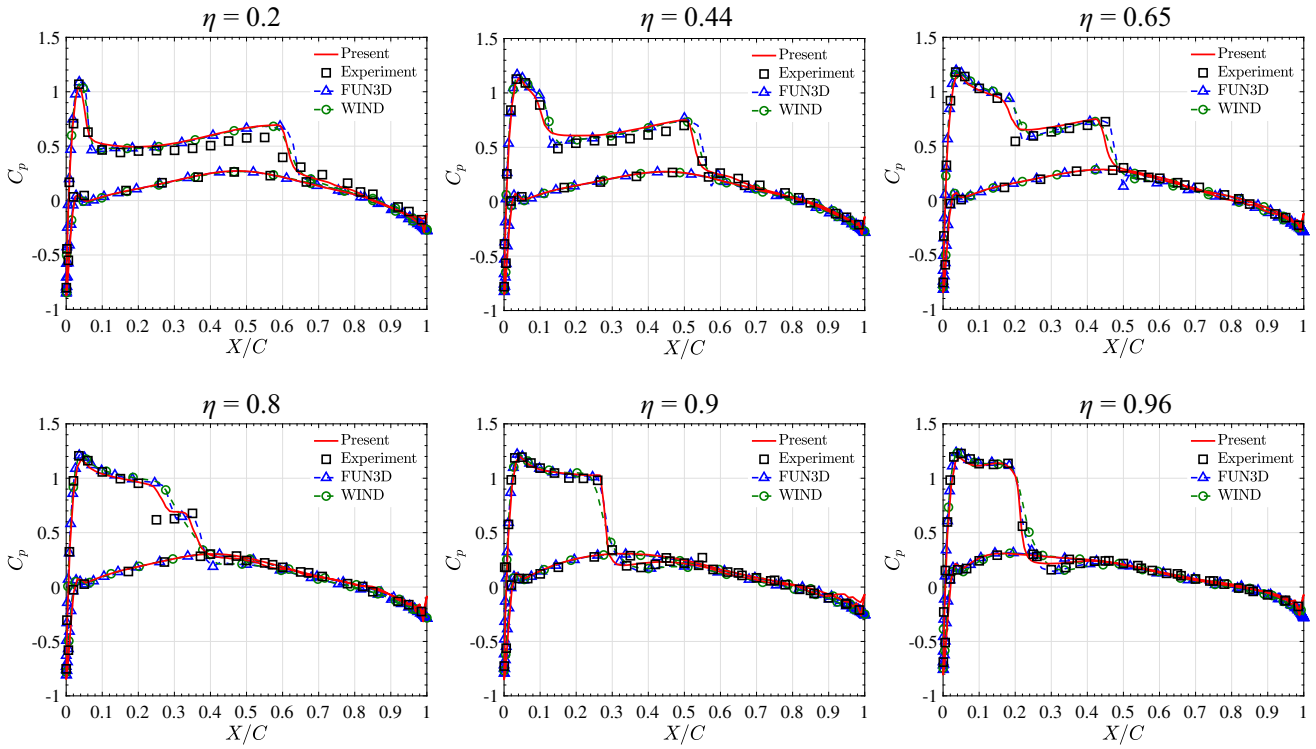

Fig. 7 Pressure coefficient plot across different spanwise cross-sections of the ONERA M6 medium level mesh (see Fig. 3 for corresponding η locations) compared with experimental data [60] and simulated results from the FUN3D [96] and WIND [97] codes

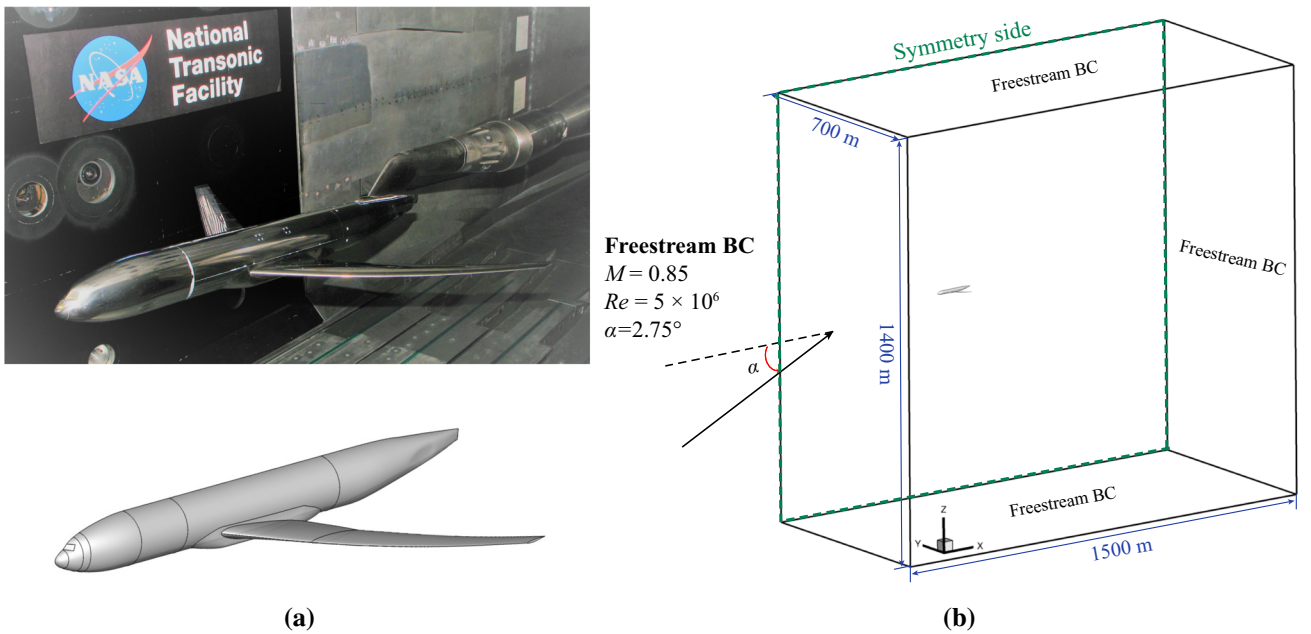

Fig. 8 (**a**) Wing-body configuration CRM experimental wind-tunnel setup [62] and right-half of the CAD geometry model used to perform the CFD simulation. (**b**) Computational domain and boundary conditions

from the AIAA workshop website [98]. Figure 9 shows the unstructured mesh discretization of the computational domain with additional enlarged views of the CRM and the wing section. The computational mesh is comprised of 12,818,968 linear elements. The size of the first element in the wall-normal direction is 0.006 m, and 12 layers of boundary-layer elements were generated with a growth ratio of 1.2. On the surface of the wing, the no-slip boundary conditions

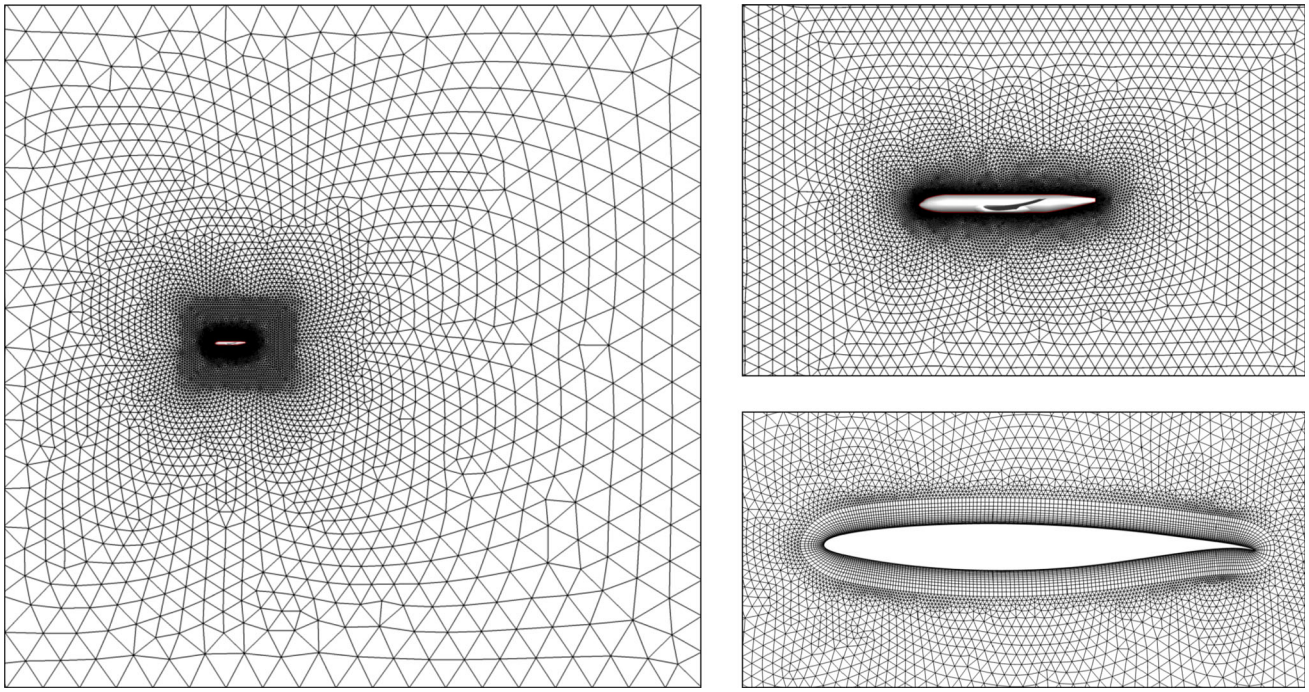

Fig. 9 Computational mesh and near-surface mesh discretization for the CRM wing-body configuration

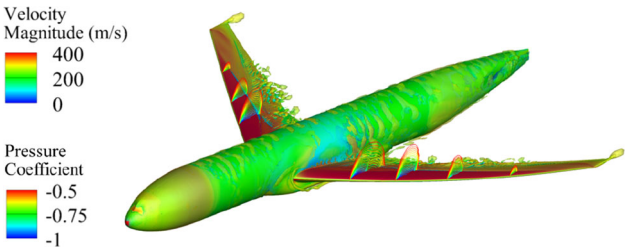

Fig. 10 Vorticity isosurfaces colored by velocity magnitude around the CRM model. Line contour of the pressure coefficient slices are also plotted at different wing locations to illustrate the shock formation

are enforced weakly, while the no-penetration boundary conditions are imposed strongly. A zero heat-flux temperature boundary condition is also applied on the airfoil surface. Symmetry boundary conditions are imposed on the plane extending from the wing root. The temperature-dependent viscosity and thermal conductivity values are determined according to Eqs. (15) and (16) with $\mu_r = 1.716 \times 10^{-5}$ kg/(m·s), $T_r = 273.15$ K, $S = 110.4$ K, $Pr = 0.72$, and c_p the specific heat at constant pressure calculated based on $\gamma = 1.4$.

Figure 10 shows the vorticity isosurfaces colored by velocity magnitude around the CRM model, including the formation of the shock structures on the wing surface. Figure 11a shows the pressure coefficient contour plotted on the top and bottom surfaces of full CRM wing-body model. The pressure coefficient data at different spanwise locations on the wing are plotted in Fig. 11b and compared with the experimental data set [62,63] and the simulated results corresponding to the Spalart–Allmaras model obtained from the 6th AIAA CFD Drag Prediction Workshop [98]. Note that the CRM geometry considered here is based on a 2.75-degree aeroelastic deflection geometry model, and the simulation is performed at a 2.75-degree angle of attack. Since the experimental data obtained from the NASA NTF and 11-ft TWT are not recorded at a 2.75-degree angle of attack, the nearest angle of attack data at 2.6 and 2.86 degrees are selected and compared with the simulation results. The pressure coefficient data from the present simulations are in good agreement with the plotted experimental data. The accuracy in capturing the shock locations and pressure drops at different spanwise locations on the wing shows the effectiveness of the entropy-based discontinuity-capturing operator for three dimensional flow problems at transonic regime. The results obtained using the coarser boundary-layer mesh with 60 times larger wall spacing compared to the medium level mesh from the AIAA workshop [98] demonstrate the effectiveness of the weakly enforced essential boundary conditions in capturing the flow solutions without excessive boundary-layer refinements.

4 Conclusions

This paper presents a finite-element-based stabilized compressible flow methodology that is comprised of SUPG, weakly enforced essential boundary conditions, and an entropy-based shock-capturing operator. The accuracy of

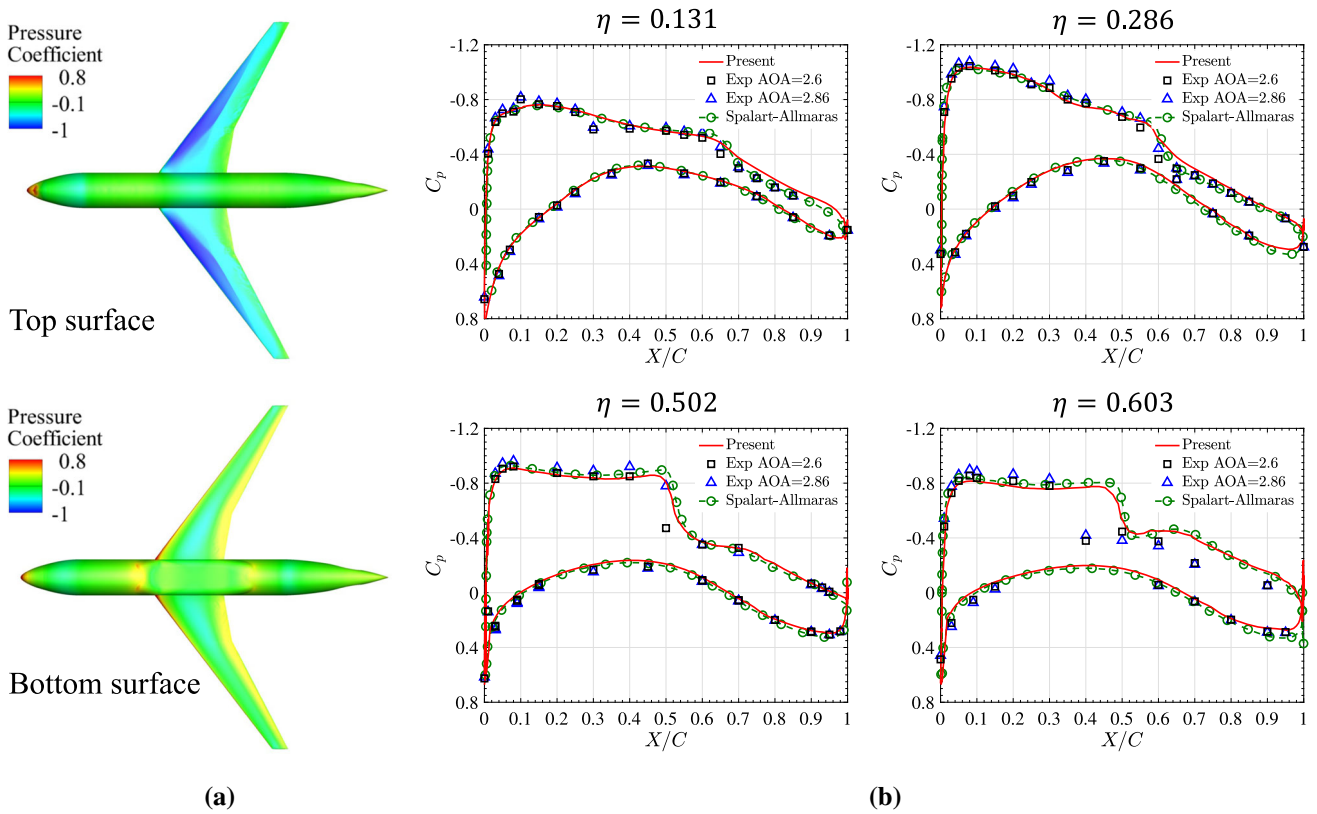

Fig. 11 (**a**) Pressure coefficient contour plot on the CRM top and bottom surfaces. (**b**) Pressure coefficient plot across different spanwise cross-sections compared with the experimental data

the formulation is demonstrated and validated through 2D and 3D benchmark cases at different flow conditions. The aerodynamic simulations were conducted at low subsonic conditions for the NACA 0012 airfoil and at a transonic condition for the RAE 2822 airfoil. 3D flow simulations of the ONERA M6 wing and NASA CRM wing-body aircraft configuration were also performed and investigated at transonic flow conditions. The pressure coefficient results obtained from both 2D and 3D simulations were in good agreement with the experimental data. The 3D simulation results obtained using the coarser boundary-layer mesh show the effectiveness of the weakly enforced essential boundary conditions in solving wall-bounded turbulent flow problems. The entropy-based discontinuity-capturing operator used in this work successfully captures smooth and accurate shock solutions in the transonic flow problems. Overall, the results presented in this paper demonstrate the accuracy and effectiveness of the stabilized finite element formulation with the weak enforcement of no-slip conditions and entropy-based discontinuity-capturing operator in simulating aircraft aerodynamics. Future work includes extending the framework to handle fluid–structure interaction with non-matching interface discretizations [99], and examining the effect of the node-numbering-invariant directional length scale [100] on these types of simulations.

Acknowledgements This work is supported by the U.S. Naval Air Systems Command (NAVAIR) under Grant No. N68335-20-C-0899. This support is gratefully acknowledged. Y. Bazilevs was also partially supported by the NSF Award No. 1854436.

References

1. Antoniadis AF, Tsoutsanis P, Drikakis D (2017) Assessment of high-order finite volume methods on unstructured meshes for RANS solutions of aeronautical configurations. Comput Fluids 146:86–104
2. Pulliam TH, Steger JL (1980) Implicit finite difference simulations of three-dimensional compressible flow. AIAA J 18:159–167
3. Ballhaus WF, Goorjian PM (1977) Implicit finite difference computations of unsteady transonic flows about airfoils. AIAA J 15:1728–1735
4. Donea J, Huerta A (2003) Finite element methods for flow problems. John Wiley & Sons, Chichester
5. Brooks AN, Hughes TJR (1982) Streamline upwind/Petrov-Galerkin formulations for convection dominated flows with particular emphasis on the incompressible Navier-Stokes equations. Comput Methods Appl Mech Eng 32:199–259

6. Hughes TJR, Tezduyar TE (1984) Finite element methods for first-order hyperbolic systems with particular emphasis on the compressible Euler equations. Comput Methods Appl Mech Eng 45:217–284
7. Hughes TJR, Mallet M (1986a) A new finite element formulation for computational fluid dynamics: III. The generalized streamline operator for multidimensional advective–diffusive systems. Comput Methods Appl Mech Eng 58:305–328
8. Hughes TJR, Franca LP, Mallet A (1986a) A new finite element formulation for computational fluid dynamics: I. Symmetric forms of the compressible Euler and Navier–Stokes equations and the second law of thermodynamics. Comput Methods Appl Mech Eng 54:223–234
9. Hughes TJR, Franca LP, Mallet M (1987) A new finite element formulation for computational fluid dynamics: VI. Convergence analysis of the generalized SUPG formulation for linear time-dependent multi-dimensional advective-diffusive systems. Comput Methods Appl Mech Eng 63:97–112
10. Shakib F, Hughes TJR, Johan Z (1991) A new finite element formulation for computational fluid dynamics: X. The compressible Euler and Navier–Stokes equations. Comput Methods Appl Mech Engrg 89:141–219
11. Le Beau GJ, Ray SE, Aliabadi SK, Tezduyar TE (1993) SUPG finite element computation of compressible flows with the entropy and conservation variables formulations. Comput Methods Appl Mech Eng 104:397–422
12. Aliabadi SK, Tezduyar TE (1993) Space-time finite element computation of compressible flows involving moving boundaries and interfaces. Comput Methods Appl Mech Eng 107:209–223
13. Tezduyar TE, Aliabadi SK, Behr M, Mittal S (1994) Massively parallel finite element simulation of compressible and incompressible flows. Comput Methods Appl Mech Eng 119:157–177
14. Hauke G, Hughes TJR (1994) A unified approach to compressible and incompressible flows. Comput Methods Appl Mech Eng 113:389–396
15. Wren GP, Ray SE, Aliabadi SK, Tezduyar TE (1995) Space-time finite element computation of compressible flows between moving components. Int J Numer Meth Fluids 21:981–991
16. Wren GP, Ray SE, Aliabadi SK, Tezduyar TE (1997) Simulation of flow problems with moving mechanical components, fluid-structure interactions and two-fluid interfaces. Int J Numer Meth Fluids 24:1433–1448
17. Ray SE, Wren GP, Tezduyar TE (1997) Parallel implementations of a finite element formulation for fluid-structure interactions in interior flows. Parallel Comput 23:1279–1292
18. Mittal S, Tezduyar T (1998) A unified finite element formulation for compressible and incompressible flows using augumented conservation variables. Comput Methods Appl Mech Eng 161:229–243
19. Ray SE, Tezduyar TE (2000) Fluid-object interactions in interior ballistics. Comput Methods Appl Mech Eng 190:363–372
20. Hauke G (2001) Simple stabilizing matrices for the computation of compressible flows in primitive variables. Comput Methods Appl Mech Eng 190:6881–6893
21. Hughes TJR, Scovazzi G, Tezduyar TE (2010) Stabilized methods for compressible flows. J Sci Comput 43:343–368
22. Takizawa K, Tezduyar TE, Kanai T (2017) Porosity models and computational methods for compressible-flow aerodynamics of parachutes with geometric porosity. Math Models Methods Appl Sci 27:771–806
23. Kanai T, Takizawa K, Tezduyar TE, Tanaka T, Hartmann A (2019) Compressible-flow geometric-porosity modeling and spacecraft parachute computation with isogeometric discretization. Comput Mech 63:301–321
24. Tezduyar TE, Park YJ (1986) Discontinuity capturing finite element formulations for nonlinear convection-diffusion-reaction equations. Comput Methods Appl Mech Eng 59:307–325
25. Hughes TJR, Mallet M, Mizukami A (1986b) A new finite element formulation for computational fluid dynamics: II. Beyond SUPG. Comput Methods Appl Mech Eng 54:341–355
26. Hughes TJR, Mallet M (1986b) A new finite element formulation for computational fluid dynamics: IV. A discontinuity-capturing operator for multidimensional advective–diffusive systems. Comput Methods Appl Mech Eng 58:329–339
27. Almeida RC, Galeão AC (1996) An adaptive Petrov-Galerkin formulation for the compressible Euler and Navier-Stokes equations. Comput Methods Appl Mech Eng 129:157–176
28. Hauke G, Hughes TJR (1998) A comparative study of different sets of variables for solving compressible and incompressible flows. Comput Methods Appl Mech Eng 153:1–44
29. Tezduyar TE, Senga M (2006) Stabilization and shock-capturing parameters in SUPG formulation of compressible flows. Comput Methods Appl Mech Eng 195:1621–1632
30. Tezduyar TE, Senga M, Vicker D (2006) Computation of inviscid supersonic flows around cylinders and spheres with the SUPG formulation and YZβ shock-capturing. Comput Mech 38:469–481
31. Tezduyar TE, Senga M (2007) SUPG finite element computation of inviscid supersonic flows with YZβ shock-capturing. Comput Fluids 36:147–159
32. Rispoli F, Saavedra R, Corsini A, Tezduyar TE (2007) Computation of inviscid compressible flows with the V-SGS stabilization and YZβ shock-capturing. Int J Numer Meth Fluids 54:695–706
33. Rispoli F, Saavedra R, Menichini F, Tezduyar TE (2009) Computation of inviscid supersonic flows around cylinders and spheres with the V-SGS stabilization and YZβ shock-capturing. J Appl Mech 76:021209
34. Rispoli F, Delibra G, Venturini P, Corsini A, Saavedra R, Tezduyar TE (2015) Particle tracking and particle-shock interaction in compressible-flow computations with the V-SGS stabilization and YZβ shock-capturing. Comput Mech 55:1201–1209
35. Takizawa K, Tezduyar TE, Otoguro Y (2018) Stabilization and discontinuity-capturing parameters for space-time flow computations with finite element and isogeometric discretizations. Comput Mech 62:1169–1186
36. Bazilevs Y, Hughes TJR (2007) Weak imposition of Dirichlet boundary conditions in fluid mechanics. Comput Fluids 36:12–26
37. Bazilevs Y, Michler C, Calo VM, Hughes TJR (2007) Weak Dirichlet boundary conditions for wall-bounded turbulent flows. Comput Methods Appl Mech Eng 196:4853–4862
38. Bazilevs Y, Michler C, Calo VM, Hughes TJR (2010) Isogeometric variational multiscale modeling of wall-bounded turbulent flows with weakly enforced boundary conditions on unstretched meshes. Comput Methods Appl Mech Eng 199:780–790
39. Xu F, Moutsanidis G, Kamensky D, Hsu M-C, Murugan M, Ghoshal A, Bazilevs Y (2017) Compressible flows on moving domains: Stabilized methods, weakly enforced essential boundary conditions, sliding interfaces, and application to gas-turbine modeling. Comput Fluids 158:201–220
40. Bazilevs Y, Akkerman I (2010) Large eddy simulation of turbulent Taylor-Couette flow using isogeometric analysis and the residual-based variational multiscale method. J Comput Phys 229:3402–3414
41. Hsu M-C, Akkerman I, Bazilevs Y (2012) Wind turbine aerodynamics using ALE-VMS: Validation and the role of weakly enforced boundary conditions. Comput Mech 50:499–511
42. Hsu M-C, Akkerman I, Bazilevs Y (2014) Finite element simulation of wind turbine aerodynamics: validation study using NREL Phase VI experiment. Wind Energy 17:461–481

43. Xu S, Gao B, Hsu M-C, Ganapathysubramanian B (2019) A residual-based variational multiscale method with weak imposition of boundary conditions for buoyancy-driven flows. Comput Methods Appl Mech Eng 352:345–368
44. Golshan R, Tejada-Martínez AE, Juha M, Bazilevs Y (2015) Large-eddy simulation with near-wall modeling using weakly enforced no-slip boundary conditions. Comput Fluids 118:172–181
45. Xu F, Schillinger D, Kamensky D, Varduhn V, Wang C, Hsu M-C (2016) The tetrahedral finite cell method for fluids: immersogeometric analysis of turbulent flow around complex geometries. Comput Fluids 141:135–154
46. Hsu M-C, Wang C, Xu F, Herrema AJ, Krishnamurthy A (2016) Direct immersogeometric fluid flow analysis using B-rep CAD models. Comput Aided Geomet Design 43:143–158
47. Xu F, Bazilevs Y, Hsu M-C (2019) Immersogeometric analysis of compressible flows with application to aerodynamic simulation of rotorcraft. Math Models Methods Appl Sci 29:905–938
48. Zhu Q, Xu F, Xu S, Hsu M-C, Yan J (2020) An immersogeometric formulation for free-surface flows with application to marine engineering problems. Comput Methods Appl Mech Eng 361:112748
49. Tezduyar T, Aliabadi S, Behr M, Johnson A, Mittal S (1993) Parallel finite-element computation of 3D flows. Computer 26(10):27–36
50. Tezduyar T, Aliabadi S, Behr M, Johnson A, Kalro V, Litke M (1996) Flow simulation and high performance computing. Comput Mech 18:397–412
51. Sturek WB, Ray S, Aliabadi S, Waters C, Tezduyar TE (1997) Parallel finite element computation of missile aerodynamics. Int J Numer Meth Fluids 24:1417–1432
52. Kozak N, Xu F, Rajanna MR, Bravo L, Murugan M, Ghoshal A, Bazilevs Y, Hsu M-C (2020) High-fidelity finite element modeling and analysis of adaptive gas turbine stator-rotor flow interaction at off-design conditions. J Mech 36:595–606
53. Kozak N, Rajanna MR, Wu MCH, Murugan M, Bravo L, Ghoshal A, Hsu M-C, Bazilevs Y (2020) Optimizing gas turbine performance using the surrogate management framework and high-fidelity flow modeling. Energies 13:4283
54. Bazilevs Y, Takizawa K, Wu MCH, Kuraishi T, Avsar R, Xu Z, Tezduyar TE (2021) Gas turbine computational flow and structure analysis with isogeometric discretization and a complex-geometry mesh generation method. Comput Mech 67:57–84
55. Codoni D, Moutsanidis G, Hsu M-C, Bazilevs Y, Johansen C, Korobenko A (2021) Stabilized methods for high-speed compressible flows: toward hypersonic simulations. Comput Mech 67:785–809
56. Ladson C. L.(1988) Effects of independent variation of Mach and Reynolds numbers on the low-speed aerodynamic characteristics of the NACA 0012 airfoil section. NASA Technical Report TM-4074, NASA,
57. Gregory N, O'Reilly C L(1970) Low-speed aerodynamic characteristics of NACA 0012 aerofoil section, including the effects of upper-surface roughness simulating hoar frost. NASA Technical Report R&M3726, NASA,
58. Harris C D(1981) Two-dimensional aerodynamic characteristics of the NACA 0012 airfoil in the Langley 8-Foot Transonic Pressure Tunnel. NASA Technical Report TM-81927, NASA,
59. Cook P H, McDonald M A, Firmin M C P(1979) Aerofoil RAE 2822 – pressure distributions, and boundary layer and wake measurements. AGARD Report AR-138, AGARD,
60. Schmitt V, Charpin F (1979)Pressure distributions on the ONERA-M6-Wing at transonic Mach numbers. AGARD Report AR-138, AGARD,
61. Vassberg J, Dehaan M, Rivers M, Wahls R Development of a Common Research Model for applied CFD validation studies. In *AIAA 2008-6919*, Honolulu, Hawaii, 2008. 26th AIAA applied aerodynamics conference
62. Rivers MB, Dittberner A (2014) Experimental investigations of the NASA Common Research Model. J Aircr 51:1183–1193
63. NASA Common Research Model. https://commonresearchmodel.larc.nasa.gov/. [Accessed 31 March 2022]
64. Le Beau G. J, Tezduyar T. E(1991) Finite element computation of compressible flows with the SUPG formulation. In *Advances in Finite Element Analysis in Fluid Dynamics*, FED-Vol.123, pp 21–27, New York, ASME
65. Hughes TJR, Feijóo GR, Mazzei L, Quincy JB (1998) The variational multiscale method-A paradigm for computational mechanics. Comput Methods Appl Mech Eng 166:3–24
66. Hughes TJR, Mazzei L, Jansen KE (2000) Large eddy simulation and the variational multiscale method. Comput Vis Sci 3:47–59
67. Bazilevs Y, Calo VM, Cottrel JA, Hughes TJR, Reali A, Scovazzi G (2007) Variational multiscale residual-based turbulence modeling for large eddy simulation of incompressible flows. Comput Methods Appl Mech Eng 197:173–201
68. Pope SB (2000) Turbulent Flows. Cambridge University Press, Cambridge
69. Hughes TJR, Oberai AA, Mazzei L (2001) Large eddy simulation of turbulent channel flows by the variational multiscale method. Phys Fluids 13:1784–1799
70. Hughes TJR, Sangalli G (2007) Variational multiscale analysis: the fine-scale Green's function, projection, optimization, localization, and stabilized methods. SIAM J Numer Anal 45:539–557
71. Masud A, Calderer R (2011) A variational multiscale method for incompressible turbulent flows: Bubble functions and fine scale fields. Comput Methods Appl Mech Eng 200:2577–2593
72. Takizawa K, Montes D, McIntyre S, Tezduyar TE (2013) Space-time VMS methods for modeling of incompressible flows at high Reynolds numbers. Math Models Methods Appl Sci 23:223–248
73. Masud A, Calderer R (2013) Residual-based turbulence models for moving boundary flows: hierarchical application of variational multiscale method and three-level scale separation. Int J Numer Meth Fluids 73(3):284–305
74. Bazilevs Y, Yan J, de Stadler M, Sarkar S (2014) Computation of the flow over a sphere at $Re = 3700$: a comparison of uniform and turbulent inflow conditions. J Appl Mech 81:121003
75. Bazilevs Y, Korobenko A, Yan J, Pal A, Gohari SMI, Sarkar S (2015) ALE-VMS formulation for stratified turbulent incompressible flows with applications. Math Models Methods Appl Sci 25:2349–2375
76. Calderer R, Zhu L, Gibson R, Masud A (2015) Residual-based turbulence models and arbitrary Lagrangian-Eulerian framework for free surface flows. Math Models Methods Appl Sci 25(12):2287–2317
77. Yang L, Badia S, Codina R (2016) A pseudo-compressible variational multiscale solver for turbulent incompressible flows. Comput Mech 58:1051–1069
78. Yan J, Korobenko A, Tejada-Martínez AE, Golshan R, Bazilevs Y (2017) A new variational multiscale formulation for stratified incompressible turbulent flows. Comput Fluids 158:150–156
79. Korobenko A, Bazilevs Y, Takizawa K, Tezduyar TE (2019) Computer Modeling of Wind Turbines: 1. ALE-VMS and ST-VMS Aerodynamic and FSI Analysis. Archives Comput Methods Eng 26:1059–1099
80. Xu S, Liu N, Yan J (2019) Residual-based variational multi-scale modeling for particle-laden gravity currents over flat and triangular wavy terrains. Computers & Fluids 188:114–124
81. Aydinbakar L, Takizawa K, Tezduyar TE, Matsuda D (2021) U-duct turbulent-flow computation with the ST-VMS method and isogeometric discretization. Comput Mech 67:823–843

82. Ravensbergen M, Helgedagsrud TA, Bazilevs Y, Korobenko A (2020) A variational multiscale framework for atmospheric turbulent flows over complex environmental terrains. Comput Methods Appl Mech Eng 368:113182
83. Zhu Q, Yan J, Tejada-Martínez AE, Bazilevs Y (2020) Variational multiscale modeling of Langmuir turbulent boundary layers in shallow water using Isogeometric Analysis. Mech Res Commun 108:103570
84. Cen H, Zhou Q, Korobenko A (2021) Simulation of stably stratified turbulent channel flow using residual-based variational multiscale method and isogeometric analysis. Computers & Fluids 214:104765
85. Aydinbakar L, Takizawa K, Tezduyar TE, Kuraishi T (2021) Space-time VMS isogeometric analysis of the Taylor-Couette flow. Comput Mech 67:1515–1541
86. Wilcox DC (2006) Turbulence Modeling for CFD, 3rd edn. DCW Industries Inc, La Cañada, CA
87. Chung J, Hulbert GM (1993) A time integration algorithm for structural dynamics with improved numerical dissipation: the generalized-α method. J Appl Mech 60:371–75
88. Jansen KE, Whiting CH, Hulbert GM (2000) A generalized-α method for integrating the filtered Navier-Stokes equations with a stabilized finite element method. Comput Methods Appl Mech Eng 190:305–319
89. Bazilevs Y, Calo VM, Hughes TJR, Zhang Y (2008) Isogeometric fluid-structure interaction: theory, algorithms, and computations. Comput Mech 43:3–37
90. Shakib F, Hughes TJR, Johan Z (1989) A multi-element group preconditioned GMRES algorithm for nonsymmetric systems arising in finite element analysis. Comput Methods Appl Mech Eng 75:415-456
91. NASA Langley Research Center Turbulence Modeling Resource: 2D NACA 0012 Airfoil Validation. https://turbmodels.larc.nasa.gov/naca0012_val.html. [Accessed 31 March 2022]
92. NPARC Alliance CFD Verification and Validation: RAE 2822 Transonic Airfoil – Study #4. https://www.grc.nasa.gov/www/wind/valid/raetaf/raetaf04/raetaf04.html. [Accessed 31 March 2022]
93. NPARC Alliance CFD Verification and Validation: RAE 2822 Transonic Airfoil. https://www.grc.nasa.gov/www/wind/valid/raetaf/raetaf.html. [Accessed 31 March 2022]
94. NASA Langley Research Center Turbulence Modeling Resource: 3D ONERA M6 Wing Validation. https://turbmodels.larc.nasa.gov/onerawingnumerics_val.html. [Accessed 31 March 2022]
95. NPARC Alliance CFD Verification and Validation: ONERA M6 Wing. https://www.grc.nasa.gov/www/wind/valid/m6wing/m6wing.html. [Accessed 31 March 2022]
96. NASA Langley Research Center Turbulence Modeling Resource: 3D ONERA M6 Wing Validation – SA-neg Model Results. https://turbmodels.larc.nasa.gov/onerawingnumerics_val_sa.html. [Accessed 31 March 2022]
97. NPARC Alliance CFD Verification and Validation: ONERA M6 Wing – Study #1. https://www.grc.nasa.gov/www/wind/valid/m6wing/m6wing01/m6wing01.html. [Accessed 31 March 2022]
98. 6th AIAA CFD Drag Prediction Workshop. https://aiaa-dpw.larc.nasa.gov/Workshop6/workshop6.html. [Accessed 31 March 2022]
99. Bazilevs Y, Hsu M-C, Scott MA (2012) Isogeometric fluid-structure interaction analysis with emphasis on non-matching discretizations, and with application to wind turbines. Comput Methods Appl Mech Eng 249–252:28–41
100. Takizawa K, Ueda Y, Tezduyar TE (2019) A node-numbering-invariant directional length scale for simplex elements. Math Models Methods Appl Sci 29:2719–2753